A Novel PRFB Decomposition for Nonstationary Time Series and Image Analysis

Pushpendra Singh*, *Member, IEEE,* Amit Singhal, Binish Fatimah, and Anubha Gupta, *Senior Member, IEEE,*

***Abstract*—This work presents a novel perfect reconstruction filter bank decomposition (PRFBD) for nonlinear and nonstationary time series and image data representation and analysis. The Fourier decomposition method (FDM), an adaptive approach wholly based on the Fourier representation, is shown to be a special case of the proposed PRFBD. The adaptive Fourier–Gauss decomposition (FGD) proposed in this work is a variation of the FDM, which is based on the FR and Gaussian filtering. Similarly, we also consider Butterworth filtering to develop adaptive Fourier–Butterworth decomposition (FBD). The proposed theory can decompose any signal (time series, image, or other data) into a set of the desired number of Fourier intrinsic band functions (FIBFs), which follow the amplitude-modulation and frequency-modulation (AM-FM) representations. A generic filterbank representation is also provided, where perfect reconstruction can be ensured for any given set of lowpass or highpass filters. We have performed an extensive analysis of both simulated and real-life data (COVID-19 pandemic, Earthquake and Gravitational waves) to demonstrate the efficacy of the proposed method. The resolution results in the time-frequency representation demonstrate that the proposed method is more promising than the state-of-the-art approaches.**

***Index Terms*—PRFB Decomposition (PRFBD), Fourier–Gauss decomposition (FGD), COVID-19, Discrete cosine transform (DCT), Fourier decomposition method (FDM).**

I. Introduction

The Fourier theory is ubiquitous in mathematics, science, engineering, and technology. Since its inception in 1807 [1]–[3], it has been used in numerous applications such as flow of heat, diffraction of electromagnetic radiation, communication, signal and image processing, acoustics, oceanography, optics and diffraction, quantum physics, music synthesis, and analysis of electrical circuits. It is one of the most important theories of modern analysis and has become an indispensable tool in treating almost every recondite question in modern physics.

Fourier representation is the most famous tool used for understanding the spectral content of a signal, extracting and interpreting information, transmitting, processing, analyzing signals and systems [4]. However, many practical signals exhibit a nonstationary character, i.e., the spectral information varies with time, wherein a specific spectral component may be significant only within a small interval of time. Therefore, it is important to develop suitable time-frequency representation (TFR) [5] of such signals that can offer insights into the different components present in the signal. TFR assists in the analysis of practical signals in a wide variety of applications, including speech processing, meteorology, and medical studies.

The short-time Fourier transform (STFT) [6] is one of the first approaches for developing TFR by computing Fourier transform over short intervals (time window) rather than considering the entire signal at once. However, the length of the time window chosen for STFT impacts the frequency resolution directly because frequency resolution is inversely proportional to time resolution. It is desirable to have a larger time window for slowly varying components and vice-a-versa. The wavelet-transform [7] provides an option to scale the basis functions (wavelets) in order to achieve the desired resolution. However, this method is heavily reliant on the choice of wavelet function as a single type of wavelet might not be effective across different categories of signals. Instead of using a fixed basis to extract signal components, researchers have explored a variety of adaptive signal decomposition methods to provide a signal-dependent algorithm for extracting relevant components [8]–[15]. Design of wavelets from a signal itself is one interesting direction [8], [9], [16], where, for example, authors in [17] demonstrated good performance in the application of ECG signal processing.

Empirical mode decomposition (EMD) [10] is the most popular and widely-used technique for the analysis of nonstationary signals. It extracts the intrinsic modes of the given signal using an iterative approach by determining the local extrema (maxima and minima) and the corresponding envelopes. It has produced satisfactory results across a variety of applications. However, EMD lacks mathematical background and suffers from the end-effect artifacts, mode-mixing, detrend uncertainty, and high sensitivity to noise. Some variants of EMD are also explored in the literature, such as ensemble EMD [11] and complete ensemble EMD [12], to address these issues pertaining to EMD by considering an ensemble of signals and then averaging the corresponding results. Although these ensemble-based approaches add to the computational complexity yet are unsuccessful in resolving all these issues. There have also been some attempts to develop adaptive methods based on the wavelet transform. Synchro-squeezed wavelet transform (SSWT) [13] considers a combination of wavelet theory and a method of reallocation in the time-frequency domain to select the significant modes of the signal. Author in [18] build empirical wavelets defined on frequency bands corresponding to the peaks in the Fourier spectrum of a signal. It provides better signal decomposition than the traditional wavelet transform, albeit at the cost of higher computational complexity. Further, Q-factor is established as

Pushpendra Singh is with the Department of Electronics and Communication Engineering, National Institute of Technology Hamirpur, Hamirpur (HP) 177005 India (e-mail: pushpendrasingh@iitkalumni.org). *Corresponding author.

Amit Singhal is with the Department of Electronics & Communication Engineering, Netaji Subhas University of Technology, Delhi, India (e-mail: singhalamit2002@gmail.com).

Binish Fatimah is with the Department of Electronics & Communication Engineering, CMR Institute of Technology, Bengaluru, India (e-mail: binish.fatimah@gmail.com).

Anubha Gupta is with the Department of Electronics and Communication Engineering, IIIT-Delhi, Delhi 110020, India (e-mail: anubha@iiitd.ac.in; Lab: http://sbilab.iiitd.edu.in/).

a significant parameter in [14], suggesting that the sub-band decomposition filters should have a low Q-factor for signals with little oscillatory behaviour and vice-a-versa. An algorithm to tune the Q-factor has been discussed. On the other hand, variational mode decomposition (VMD) is proposed in [15] to estimate the principal modes concurrently by minimizing the collective bandwidth for these modes while ensuring optimal reconstruction of the signal.

Contrary to popular belief established in these works that the Fourier methods are not suited for adaptive signal analysis of practical nonstationary signals, the Fourier decomposition method (FDM) has been proposed recently [19], [20]. The FDM has been used in many applications such as biomedical signal processing and COVID-19 pandemic modelling and prediction [21]–[28]. It can be implemented efficiently using fast Fourier transform (FFT) and has produced promising results across a wide range of applications. However, FDM is based on the rectangular zero-phase filterbank, which causes unwanted fluctuations in time or spatial domain, e.g., oscillations in a trend estimation from time series and ringing effect in an image decomposition. Therefore, there is a need to extend the FDM theory [29] to be used across a variety of filterbanks exhibiting smoother transition bands for comprehensive signal analysis while ensuring perfect reconstruction of the original signal without the need for an exclusive filtering stage for signal synthesis. In this work, we develop a novel method to derive perfect reconstruction filterbanks, and it is shown that many existing signal decomposition schemes, such as FDM, EMD, EWT, can be considered as special cases of the generalized model proposed here. In contrast to the FDM, we propose an adaptive Fourier–Gauss decomposition, since the Gaussian function has a minimum time-width product and thus provides excellent localization properties in both time and frequency and efficient utilization of the available bandwidth of the communication channel. Results indicate superior performance of the proposed method as compared to the popular existing methods.

The main contributions of this study are summarized as follows:

1) Generalized approach is proposed for the design of a perfect reconstruction filterbank (PRFB). The PRFB can be designed using a set of lowpass (or highpass) filters with the desired overlap among adjacent bands by suitably selecting the cut-off and stopband edge frequencies and stopband attenuation.
2) An adaptive Fourier–Gauss decomposition (FGD) is defined using the PRFB based on the generalized Gaussian model.
3) An adaptive Fourier–Butterworth decomposition (FBD) is also developed considering the maximally flat Butterworth filters.
4) Additionally, four different types of filters are also proposed to obtain the desired PRFB.
5) A number of methods are discussed for obtaining desired cut-off frequencies (such as equal frequency bands, dyadic bands, constant high or low resonance bands, variable resonance bands, and other desired bands) that can be adopted in the proposed PRFB.
6) The Gram–Schmidt orthogonalization method (GSOM) is incorporated in the proposed approach such that the set of Fourier intrinsic band functions (FIBFs), obtained using the PRFB, are complete as well as orthogonal. Thus the proposed method preserves the energy of the signal in the decomposition and time-frequency representation.

The proposed methods are able to decompose any time series, image, and other data into a set of FIBFs, which are local, adaptive, complete, and orthogonal by virtue of the proposed PRFB and GSOM.

Notations: This work uses small letters for time-domain signals (e.g., $d(t)$–continuous time and $d[n]$–discrete time), and capital letters for frequency-domain signals (e.g., $D(f)$–continuous frequency and $D[k]$–discrete frequency).

II. The Fourier Decomposition Method

The FDM is an adaptive approach for nonlinear and nonstationary time series decomposition and analysis using the zero-phase filtering (ZPF) [19]. It decomposes a given data (or signal) into a constant and a set of FIBFs, which are band-limited AM-FM components. The FIBFs are zero-mean, adaptive, complete, local, and energy preserving (EP), i.e., orthogonal or linearly-independent non-orthogonal yet EP (LINOEP). The FDM can be implemented using ZPF based on Fourier representations such as discrete Fourier transform (DFT), discrete cosine transforms (DCTs) and discrete sine transforms (DSTs); finite impulse response (FIR) and infinite impulse response (IIR) filters, or any other approach. In this work, we propose the FDM using the DCT and Gaussian filtering and designate it as adaptive Fourier–Gauss Decomposition (FGD). Let $d[n]$ be a data sequence of length N. The DCT type-2 of $d[n]$ is defined as [30]

$$D[k] = \sqrt{\frac{2}{N}}\sigma_k \sum_{n=0}^{N-1} d[n] \cos\left(\frac{\pi k(2n+1)}{2N}\right),\ 0 \le k \le N-1, \tag{1}$$

where $\sigma_k = \frac{1}{\sqrt{2}}$ for $k = 0$ and $\sigma_k = 1$ for $k \neq 0$. The original sequence $d[n]$ can be recovered using the inverse DCT (IDCT) defined as

$$d[n] = \sqrt{\frac{2}{N}} \sum_{k=0}^{N-1} \sigma_k D[k] \cos\left(\frac{\pi k(2n+1)}{2N}\right),\ 0 \le n \le N-1. \tag{2}$$

The set of orthogonal cosine basis functions $\cos\left(\frac{\pi k(2n+1)}{2N}\right)$ of the DCT (1) are a class of discrete Chebyshev polynomials [30]. A set of M FIBFs from the data $d[n]$ can be obtained as [19], [20]

$$d[n] = \sqrt{\frac{2}{N}} \sum_{k=0}^{N-1} \sigma_k D[k] \cos\left(\frac{\pi k(2n+1)}{2N}\right) = d_0 + \sum_{i=1}^{M} d_i[n], \tag{3}$$

where $M << N$, $d_0 = \sqrt{\frac{2}{N}}\sigma_0 D[0]$, $d_1[n] = \sqrt{\frac{2}{N}} \sum_{k=1}^{K_1} \sigma_k D[k] \cos\left(\frac{\pi k(2n+1)}{2N}\right)$, $d_2[n] = \sqrt{\frac{2}{N}} \sum_{k=(K_1+1)}^{K_2} \sigma_k D[k] \cos\left(\frac{\pi k(2n+1)}{2N}\right)$, $\ldots$, $d_M[n] = \sqrt{\frac{2}{N}} \sum_{k=(K_{M-1}+1)}^{N-1} \sigma_k D[k] \cos\left(\frac{\pi k(2n+1)}{2N}\right)$. In other words, FIBFs are obtained by considering the rectangular window $G_i[k]$ based filtering as

$$d_i[n] = \sqrt{\frac{2}{N}} \sum_{k=1}^{N-1} \sigma_k D[k] G_i[k] \cos\left(\frac{\pi k(2n+1)}{2N}\right), \tag{4}$$

where

$$G_i[k] = \begin{cases} 1, & K_{i-1}+1 \le k \le K_i, \\ 0, & \text{otherwise}, \end{cases} \tag{5}$$

with $K_0 = 0$, $K_M = N-1$ and $i = 1, 2, \ldots, M$. Based on the requirements of the application under consideration, the desired values of $K_1, K_2, \ldots, K_{M-1}$ can be selected.

There are many applications where we are interested in the estimation of trend $\tau[n]$ and variability $v[n]$ from the data $d[n]$ such that

$$d[n] = \tau[n] + v[n], \tag{6}$$

where $\tau[n] = \sqrt{\frac{2}{N}} \sum_{k=0}^{N-1} \sigma_k D[k] G[k] \cos\left(\frac{\pi k(2n+1)}{2N}\right)$ and $v[n] = \sqrt{\frac{2}{N}} \sum_{k=0}^{N-1} \sigma_k D[k] H[k] \cos\left(\frac{\pi k(2n+1)}{2N}\right)$; $G[k]$ and $H[k]$ are the lowpass and highpass filters, respectively, which are defined as

$$G[k] = \begin{cases} 1, & 0 \le k \le K, \\ 0, & K+1 \le k \le N-1, \end{cases} \quad \text{and} \quad H[k] = 1 - G[k], \tag{7}$$

where various values of K can be selected to obtain the desired trends and variabilities in respective time-scales. From (3) and (6), it can be shown that $\sum_{n=0}^{N-1} d[n] = N d_0 = \sum_{n=0}^{N-1} \tau[n]$ as $\sum_{n=0}^{N-1} v[n] = \sum_{n=0}^{N-1} d_i[n] = 0, \forall\, i \neq 0$. For example, if $d[n]$ is the data of COVID-19 which represents cases/deaths per day, then sum of the estimated trend represents the total number of cases/deaths. The fast Fourier transform (FFT) algorithm [31] can be used to efficiently implement FDM based on the DCT.

The main problem with FDM is the use of rectangular windows that causes unnecessary fluctuations/oscillations in the estimated trends due to the presence of sharp discontinuities at both ends. These fluctuations create problems in the modeling and prediction of a physical phenomenon such as the COVID-19 pandemic. To overcome this issue, we propose the FGD and other similar techniques.

III. Proposed Methods

In this section, we present the FGD and FBD and also provide some other suggestions for designing the filters suitable for the representation and analysis of one (or two) dimensional signals (or images). Before discussing these, we propose a generalized algorithm for designing a perfect reconstruction (PR) filterbank (PRFB) and various methods of selecting the appropriate cut-off frequencies.

A. Perfect Reconstruction Filterbank

In this subsection, we propose a PRFB based on Theorem 1 as follows.

Theorem 1. *If there is a set of $M \ge 1$ lowpass filters $\{G_1[k], G_2[k], \ldots, G_M[k]\}$ having cut-off frequencies $\{f_{c_1}, f_{c_2}, \ldots, f_{c_M}\}$, respectively, such that $0 < f_{c_1} < f_{c_2} < \cdots < f_{c_M} < F_s/2$. Then, there exists a set of $(M+1)$ filters $\{H_1[k], H_2[k], \ldots, H_M[k], H_{M+1}[k]\}$ that form a PRFB, i.e.,*

$$\sum_{\ell=1}^{M+1} H_\ell[k] = 1, \qquad \forall\, k, \tag{8}$$

and are derived from $\{G_1[k], \ldots, G_M[k]\}$ as

$$\begin{aligned} H_1[k] &= G_1[k], \\ H_2[k] &= (1 - G_1[k]) G_2[k], \\ H_3[k] &= (1 - G_1[k])(1 - G_2[k]) G_3[k], \\ &\vdots \\ H_M[k] &= (1 - G_1[k])(1 - G_2[k]) \ldots (1 - G_{M-1}[k]) G_M[k], \\ H_{M+1}[k] &= (1 - G_1[k])(1 - G_2[k]) \ldots (1 - G_{M-1}[k]) \times \\ &\qquad (1 - G_M[k]), \end{aligned} \tag{9}$$

where $H_1[k]$ is a lowpass (LP) filter, $H_2[k], H_3[k], \ldots, H_M[k]$ are bandpass (BP) filters, and $H_{M+1}[k]$ is a highpass (HP) filter.

Proof. Refer to top-left of Figure 1(a) for $G_\ell[k]$ and bottom-left of Figure 1(a) for $H_\ell[k]$.

Base Cases: (i) For $M = 1$, theorem is true because

$$\begin{aligned} H_1[k] &= G_1[k], \\ H_2[k] &= 1 - G_1[k], \\ \implies H_2[k] + H_1[k] &= 1, \end{aligned}$$

and (ii) for $M = 2$, theorem is true because

$$\begin{aligned} H_1[k] &= G_1[k], \\ H_2[k] &= (1 - G_1[k]) G_2[k], \\ H_3[k] &= (1 - G_1[k])(1 - G_2[k]), \\ \implies H_3[k] + H_2[k] + H_1[k] &= 1. \end{aligned}$$

Generic Case: Considering now a generic value for M, the proof of this theorem can be easily obtained by addition of filters (9) in reverse order as follows:

$$\begin{aligned} H_{M+1}[k] + H_M[k] &= (1 - G_1[k])(1 - G_2[k]) \ldots \\ &\qquad (1 - G_{M-1}[k]), \\ H_{M+1}[k] + H_M[k] + H_{M-1}[k] &= (1 - G_1[k])(1 - G_2[k]) \ldots \\ &\qquad (1 - G_{M-2}[k]), \\ &\vdots \\ H_{M+1}[k] + \cdots + H_2[k] &= (1 - G_1[k]), \\ H_{M+1}[k] + \cdots + H_2[k] + H_1[k] &= 1, \qquad \forall\, k. \end{aligned} \tag{10}$$

The last step follows from (9) since $H_1[k] = G_1[k]$. Thus, the theorem is true for all integers $M \ge 1$, which completes the proof. □

Remark. *The PRFB presented in* (8) *and* (9) *is generic in nature, although it has been used in this work for the design of one dimensional discrete zero-phase filterbank. In other words, $G_1, G_2, \ldots, G_M$ can be any complex-valued multidimensional (discrete or continuous) functions, for which a set of PR functions $H_1, H_2, \ldots, H_M, H_{M+1}$ can be obtained.*

One can observe that $\sum_{\ell=1}^{M+1} H_\ell[k] = 1, \quad \forall\, k \iff \sum_{\ell=1}^{M+1} h_\ell[n] = \delta[n]$ where $h_\ell[n] = \text{IDCT}(H_\ell[k])$, is the impulse response of the ℓ-th filter. Using the filters $H_\ell[k]$, as shown in Figure 2 and Figure 3, we obtain the decomposition of a signal $d[n]$ as:

$$d[n] = \sum_{\ell=1}^{M+1} d_\ell[n], \tag{11}$$

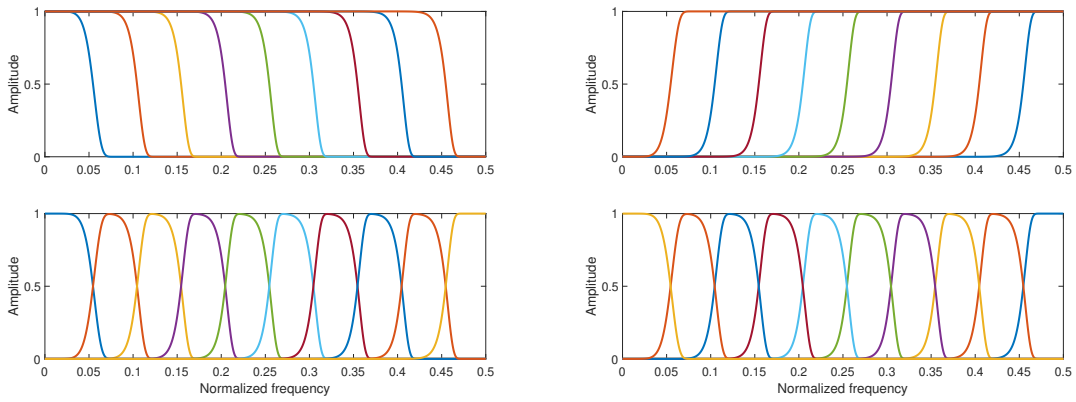

Fig. 1. A PRFB (8) obtained from (9) with $F_s = 1$ using the generalized Gaussian (a) LP filters $\{G_\ell\}_{\ell=1}^{9}$ (top) and corresponding $\{H_\ell\}_{\ell=1}^{10}$ (bottom), and (b) HP filters $\{G_\ell\}_{\ell=1}^{9}$ (top) and corresponding $\{H_\ell\}_{\ell=1}^{10}$ (bottom).

where the components $\{d_\ell[n] = \text{IDCT}(D[k]H_\ell[k]),\ 1 \leq \ell \leq M+1\}$ are generally not orthogonal. Hence, the energy of a signal is not preserved in this decomposition.

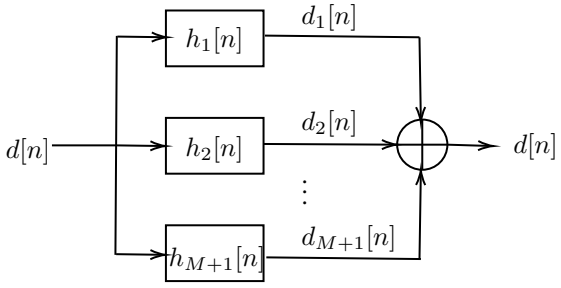

Fig. 2. The proposed PRFB such that $\sum_{\ell=1}^{M+1} h_\ell[n] = \delta[n]$.

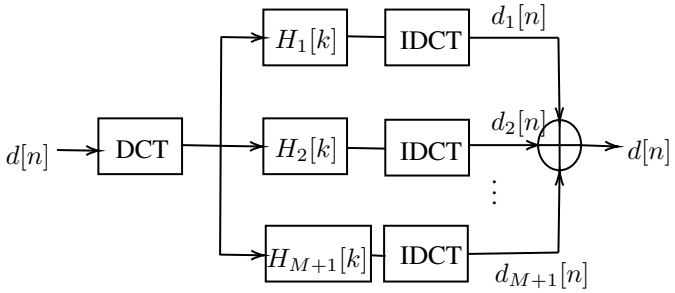

Fig. 3. An efficient implementation of the proposed PRFB using DCT, where DFT can also be used. The PR is obtained by ensuring $\sum_{i=1}^{M+1} H_i[k] = 1\ \forall k$.

Since Gram-Schmidt orthogonalization method (GSOM) is a well known process for orthogonalizing a set of linearly independent (LI) vectors in an inner product space, it can be used to achieve orthogonality among the signal components. Let $D = \{d_1[n], d_2[n], ..., d_{M+1}[n]\}$ be a set of $(M+1)$ LI vectors. A set of orthogonal vectors $S = \{s_1[n], s_2[n], ..., s_{M+1}[n]\}$ spanning the same space can be generated using GSOM as follows:

$$s_k[n] = d_k[n] - \sum_{i=1}^{k-1} c_{ki} s_i[n] \Leftrightarrow \begin{bmatrix} d_1[n] \\ d_2[n] \\ \vdots \\ d_{M+1}[n] \end{bmatrix} = \begin{bmatrix} 1 & 0 & \dots & 0 \\ c_{21} & 1 & \dots & 0 \\ \vdots & \vdots & \ddots & \vdots \\ c_{(M+1)1} & c_{(M+1)2} & \dots & 1 \end{bmatrix} \begin{bmatrix} s_1[n] \\ s_2[n] \\ \vdots \\ s_{M+1}[n] \end{bmatrix}, \quad (12)$$

where the inner product $\langle s_k[n], s_i[n] \rangle = 0$, for $k \neq i$ and $k = 1, 2, \dots, M+1$. The coefficients c_{ki} are obtained as $c_{ki} = \sum_{n=0}^{N-1} d_k[n] s_i[n] / \sum_{n=0}^{N-1} s_i^2[n]$ for $i = 1, 2, \dots, M+1$, where $k \geq i$ and N is the length of these signals. By considering the sum of all the $(M+1)$ equations of (12), we obtain

$$\sum_{i=1}^{M+1} d_i[n] = \sum_{i=1}^{M+1} c_i s_i[n], \quad (13)$$

where $c_i = \sum_{k=i}^{M+1} c_{ki}$, which is the sum of the i-th column of the coefficient matrix of (12). Finally, we obtain a decomposition of signal $d[n]$ into a set of orthogonal FIBFs $\{\tilde{d}_1[n], \tilde{d}_2[n], ..., \tilde{d}_{M+1}[n]\}$ with PR as

$$d[n] = \sum_{i=1}^{M+1} \tilde{d}_i[n], \quad \text{where} \quad \tilde{d}_i[n] = c_i s_i[n]. \quad (14)$$

Corollary 1.1. *Let us consider a set of M number of high-pass filters $\{G_1[k], G_2[k], \dots, G_M[k]\}$ with cut-off frequencies $\{f_{c_1}, f_{c_2}, \dots, f_{c_M}\}$ such that $0 < f_{c_M} \cdots < f_{c_2} < f_{c_1} < F_s/2$. Then, the set of filters represented in (8) form a PRFB, where $H_1[k]$ is a HP filter, $H_2[k], H_3[k], \dots, H_M[k]$ are BP filters, and $H_{M+1}[k]$ is a LP filter.*

For an example, one may refer to Figure 1(b).

B. Selection of Cut-off Frequencies

The strength and utility of signal decomposition techniques also depends on the right choice of cut-off frequencies. The

basic idea is to divide the entire frequency range $[0, F_s/2]$ into a set of desired bands. Let $\{f_{c_1}, f_{c_2}, \ldots, f_{c_M}\}$ be a set of cut-off frequencies such that $0 < f_{c_1} < f_{c_2} < \cdots < f_{c_M}$ for a set of frequency bands $\{[0, f_{c_1}), [f_{c_1}, f_{c_2}), \ldots, [f_{c_{M-1}}, f_{c_M}]\}$ where $f_{c_M} = F_s/2$. We can adopt the following strategies for selecting the cut-off frequencies:

1) Equal resonance bands: The quality factor (Q-factor) is defined as the ratio of centre frequency ($c_{f_i} = (f_{c_{i+1}} + f_{c_i})/2$) to bandwidth (BW), i.e.,
$$\begin{aligned} Q &= c_{f_i}/(f_{c_{i+1}} - f_{c_i}), \\ &= \frac{1}{2}\left(\frac{f_{c_{i+1}} + f_{c_i}}{f_{c_{i+1}} - f_{c_i}}\right), \\ \implies \quad f_{c_i} &= \left(\frac{2Q-1}{2Q+1}\right) f_{c_{i+1}}, \quad Q > \frac{1}{2}, \end{aligned} \tag{15}$$
for $i = M-1, \ldots, 2, 1$. The dyadic cut-off frequencies correspond to $Q = 1.5$. Depending on the problem under analysis, we can select the desired value of Q. The greater the value of Q (i.e., high resonance–more sustained oscillations), the narrower the band. Further, we can vary the value of Q for each band and can obtain variable Q-factor decomposition.
2) p-adic frequency bands: We can divide the frequency range $[0, F_s/2]$ as $f_{c_{M-i}} = \frac{F_s}{2} \times \frac{1}{p^i}$, where $p > 1$ is a real number, and $i = 0, 1, 2, 3, \ldots, M-1$. Here, $p = 2$ corresponds to a dyadic filterbank.
3) Uniform frequency bands: In this case, we can simply divide the $[0, F_s/2]$ into a set of M bands with equal bandwidth, i.e., $f_{c_i} = f_{c_{i-1}} + [F_s/(2M)]$ where $f_{c_0} = 0$, and $i = 1, 2, \ldots, M$.
4) User-defined bands: In certain applications, the user can be given the flexibility to select the desired number of bands and their cut-off frequencies $\{f_{c_1}, f_{c_2}, \ldots, f_{c_M}\}$. If there is any prior knowledge about the spectral content of the signal, the user can utilize that knowledge to select the cut-off frequencies.
5) Signal-dependent adaptive bands: The most popular technique for the selection of frequency bands is to extract the cut-off frequencies from the signal itself. Such algorithms exhibit two desirable properties: adaptive and signal-dependent. There are multiple ways of achieving this, such as (i) we can obtain the frequencies corresponding to peaks and/or troughs of the magnitude spectrum of a signal using the Fourier transform and decide the cut-off frequencies, (ii) obtaining equal energy bands using the Fourier spectrum, or (iii) obtain Fourier intrinsic band functions [19] using low-to-high or high-to-low frequency scans.

C. Proposed Filtering Strategies

1) Gaussian Filters: The impulse response of the Gaussian lowpass filter (GLPF) is defined as
$$g(t) = \frac{1}{\sigma\sqrt{2\pi}} \exp\left(\frac{-t^2}{2\sigma^2}\right), \tag{16}$$
where σ is the standard deviation (SD). The Gaussian filter (16) can be represented in the Fourier domain as
$$G(f) = \exp\left(-2\pi^2\sigma^2 f^2\right) = \exp\left(\frac{-f^2}{2\hat{\sigma}^2}\right), \tag{17}$$
where $\hat{\sigma}$ is the SD in frequency domain, and the time-bandwidth product, $\sigma\,\hat{\sigma} = \frac{1}{2\pi}$, which is optimal (minimum) for the Gaussian function. For all other functions, $\sigma\,\hat{\sigma} > \frac{1}{2\pi}$. The cut-off frequency f_c at which $G(f_c) = \frac{1}{\sqrt{a}}$ is obtained from (17) as $f_c = \hat{\sigma}\sqrt{\ln(a)}$ for $a > 1$. It is half power or -3 dB bandwidth for $a = 2$. The lowpass Gaussian filter (LP-GF) (17) and the corresponding highpass Gaussian filter (HP-GF) $H(f)$ can be written in terms of the cut-off frequency f_c as
$$G(f) = \exp\left(-\left(\frac{f}{f_c}\right)^2 \ln\left(\sqrt{a}\right)\right) \quad \text{and} \quad H(f) = 1 - G(f), \tag{18}$$
respectively. In order to obtain the same f_c for both the LPF and HPF, we use $a = 4$ which corresponds to -6 dB bandwidth. With a sampling frequency of F_s, the cut-off frequency must satisfy the relation $f_c \leq F_s/2$ in order to obtain the discrete counterpart of this filter.

Therefore, we obtain the proposed FGD by using the following LPF and HPF in (7):
$$G[k] = \exp\left(-\left(\frac{k}{k_c}\right)^2 \ln\left(\sqrt{a}\right)\right) \quad \text{and} \quad H[k] = 1 - G[k], \tag{19}$$
respectively, with $k = 0, 1, \ldots, N-1$, and $k_c = 2f_c(N-1)/F_s$, where F_s is the sampling frequency. For example, Figure 4 (top) shows four pairs of the Gaussian LPF and HPF with cut-off frequencies $f_{c_1} = F_s/4$, $f_{c_2} = F_s/8$, $f_{c_3} = F_s/16$, $f_{c_4} = F_s/32$, $F_s = 1$. Thus, the maximum normalized frequency is 0.5, which corresponds to $F_s/2$. The Gaussian LPF and HPF obtained using (19) provide good resolution/separation in the low-frequency band and poor resolution/roll-off in the high-frequency band. This is required in many of the applications, wherein most of the energy is concentrated in the low frequencies. However, if an application requires good resolution in the high-frequency band, we can use the following filters
$$G[k] = 1 - H[k], \quad H[k] = \exp\left(-\left(\frac{N-1-k}{N-1-k_c}\right)^2 \ln\left(\sqrt{a}\right)\right), \tag{20}$$
which provides poor resolution/roll-off in the low frequency band. For example, these LPF and HPF are shown in Figure 4 (bottom) with cut-off frequencies $f_{c_1} = F_s/4$, $f_{c_2} = 3F_s/8$, $f_{c_3} = 7F_s/16$, and $f_{c_4} = 15F_s/32$. Since all these filter are zero-phase, filter coefficients are non-negative real numbers, i.e., $G[k] \in \mathbb{R}_{\geq 0}$ (or $\mathbb{R}^+$) and $H[k] \in \mathbb{R}_{\geq 0}$.

We can use the generalized Gaussian filter to resolve the poor roll-off of the filters discussed in (19) and (20). The generalized Gaussian LPF (GG-LPF) can be defined as
$$G(f) = \exp\left(-\left(\frac{|f-\mu|}{\alpha}\right)^m\right), \tag{21}$$
where both the scale parameter α and the shape parameter m are positive real numbers, while the location parameter $\mu \in \mathbb{R}$. The GG-LPF (21) and GG-HPF with $\mu = 0$ can be written as
$$G(f) = \exp\left(-\left|\frac{f}{f_c}\right|^m \ln\left(\sqrt{a}\right)\right), \tag{22}$$
$$G[k] = \exp\left(-\left|\frac{k}{k_c}\right|^m \ln\left(\sqrt{a}\right)\right) \quad \text{and} \quad H[k] = 1 - G[k]. \tag{23}$$

Algorithm 1: Proposed FGD algorithms to obtain FIBFs $d_i[n]$ from data $d[n]$ such that $d[n] = \sum_{i=1}^{M} d_i[n] + \tau[n]$ in order of: (OPTION-A) highest to lowest frequency components, and (OPTION-B) lowest to highest frequency components. In these algorithms, we have used the normalized sampling frequency, i.e, $F_s = 1$, which can be replaced by the actual value, as per the application.

% OPTION-A, set desired cut-off frequencies s.t.;
% $0 < f_{c_M} < \cdots < f_{c_2} < f_{c_1} < F_s/2$;
$F_s = 1$; $N = \text{length}(d[n])$;
$k_{c_1} = 2f_{c_1}(N-1)/F_s$;
$D[k] = \text{DCT}(d[n])$ from (1);
Obtain LP-GF $G_1[k]$ with k_{c_1} from (19);
$T_1[k] = D[k]G_1[k]$;
$D_1[k] = D[k](1 - G_1[k])$;
$d_1[n] = \text{IDCT}(D_1[k])$ from (2);
for $i = 2$ *to* M **do**
  $k_{c_i} = 2f_{c_i}(N-1)/F_s$;
  Obtain LP-GF $G_i[k]$ with k_{c_i} from (19);
  $T_i[k] = T_{i-1}[k]G_i[k]$;
  $D_i[k] = T_{i-1}[k](1 - G_i[k])$;
  $d_i[n] = \text{IDCT}(D_i[k])$ from (2);
$\tau[n] = \text{IDCT}(T_M[k])$;

% OPTION-B, set desired cut-off frequencies s.t.;
% $0 < f_{c_1} < f_{c_2} < \cdots < f_{c_M} < F_s/2$;
$F_s = 1$; $N = \text{length}(d[n])$;
$k_{c_1} = 2f_{c_1}(N-1)/F_s$;
$D[k] = \text{DCT}(d[n])$ from (1);
Obtain LP-GF $G_1[k]$ with k_{c_1} from (19);
$T_1[k] = D[k]G_1[k]$;
$D_1[k] = D[k](1 - G_1[k])$;
$\tau[n] = \text{IDCT}(T_1[k])$ from (2);
for $i = 2$ *to* M **do**
  $k_{c_i} = 2f_{c_i}(N-1)/F_s$;
  Obtain LP-GF $G_i[k]$ with k_{c_i} from (19);
  $T_i[k] = D_{i-1}[k]G_i[k]$;
  $D_i[k] = D_{i-1}[k](1 - G_i[k])$;
  $d_{i-1}[n] = \text{IDCT}(T_i[k])$ from (2);
$d_M[n] = \text{IDCT}(D_M[k])$;

A set of nine GG-LPF (with normalized frequencies $f_c = 0.05, 0.1, 0.15, 0.2, 0.25, 0.3, 0.35, 0.4, 0.45$, varying $m = 8, 16, 24, 32, 40, 48, 56, 64, 72$ and $a = 2$) and a set of nine GG-HPF are shown in top-left and top-right of Figure 1, respectively.

Let f_s and G_s be the stopband edge frequency and stopband attenuation (SBA) of the GG-LPF, respectively, where $f_s > f_c$, $G_s < 1$, and the transition bandwidth is $(f_s - f_c)$ Hz. We can select the desired design parameters f_c, f_s, and G_s (e.g., $G_s = 10^{-6}$ corresponds to -120 dB) and obtain the value of shape parameter m as

$$G(f_s) = G_s = \exp\left(-\left|\frac{f_s}{f_c}\right|^m \ln\left(\sqrt{a}\right)\right), \tag{24}$$

$$\text{and thus} \quad m = \log\left(-\frac{\ln(G_s)}{\ln\left(\sqrt{a}\right)}\right) \Big/ \log\left(\left|\frac{f_s}{f_c}\right|\right). \tag{25}$$

The proposed FGD is summarized in Algorithm 1 (OPTION-A), which decomposes data $d[n]$ such that

$$d[n] = \sum_{i=1}^{M} d_i[n] + \tau[n], \tag{26}$$

where $\tau[n]$ is the trend of data $d[n]$. The FIBFs and trend $\{d_1[n], d_2[n], \ldots, d_M[n], \tau[n]\}$ are arranged in the order of highest to lowest frequency components. If we add all $T_i[k]$ and $D_i[k]$ in Algorithm 1 (OPTION-A), we obtain $\sum_{i=1}^{M}(T_i[k] + D_i[k]) = D[k] + \sum_{i=1}^{M-1} T_i[k]$, which implies that $D[k] = T_M[k] + \sum_{i=1}^{M} D_i[k]$, where trend $T_M[k] = T_{M-1}[k]G_M[k] = D[k]G_1[k] \ldots G_M[k]$, i.e., the trend is obtained by filtering the data from all the filters successively. Similarly, there is an another version of the GFD, Algorithm 1 (OPTION-B) that produces trend and FIBFs $\{\tau[n], d_1[n], d_2[n], \ldots, d_M[n]\}$, which are arranged in order of the lowest to highest frequency components.

2) Butterworth Filter: It is designed to obtain maximally flat (i.e., no ripples) frequency response in the passband [32]. The zero-phase lowpass Butterworth filter (LPBF) and highpass Butterworth filter (HPBF) of p-th order can be defined as

$$B(f) = \frac{1}{\sqrt{1 + \left(\frac{f}{f_c}\right)^{2p}(a-1)}},\ f_c = (a-1)^{\frac{1}{2p}},\ a > 1,$$
$$\text{and} \quad C(f) = 1 - B(f), \tag{27}$$

respectively, where the half-power (-3 dB) bandwidth of the filter corresponds to $a = 2$. For smaller values of p, the cut-off is less sharp. As p approaches infinity, the filter response approaches a rectangle function, wherein frequencies below f_c will be passed, while frequencies above f_c will be suppressed.

3) Exponentially decaying filter: If we consider a function and its FT as

$$g(t) = \left(\frac{1}{\pi}\frac{\alpha}{\alpha^2 + t^2}\right),\ G(f) = \exp(-\alpha\,|2\pi f|),\ \alpha \geq 0, \tag{28}$$

then we can define LPF and HPF (similar to FGD (18)) as below:

$$G(f) = \exp\left(-\left|\frac{f}{f_c}\right| \ln\left(\sqrt{a}\right)\right), \tag{29}$$

$$\text{and} \quad H(f) = 1 - G(f), \qquad f_c = \frac{1}{2\pi\alpha}\ln\left(\sqrt{a}\right), \tag{30}$$

respectively. In order to obtain the same f_c for both the LP and HP filters, we use $a = 4$ which corresponds to -6 dB bandwidth.

4) Raised-cosine filter: Raised-cosine filters are generally proposed as popular alternatives to rectangular filters because they offer a faster decay of the impulse response, thereby, making it more compact. An LP raised cosine filter is expressed as

$$G(f) = \begin{cases} 1, & |f| \leq f_c(1-\alpha), \\ \frac{1}{2}\left[1 + \cos\left(\frac{\pi(|f| - f_c(1-\alpha))}{2\alpha f_c}\right)\right], & \\ f_c(1+\alpha) < |f| \leq f_c(1+\alpha), & \\ 0, & \text{otherwise}, \end{cases} \tag{31}$$

$$H(f) = 1 - G(f), \tag{32}$$

where the factor $\alpha \in [0, 1]$ controls the transition bandwidth, with smaller α providing sharper cut-off and vice-a-versa. The magnitude of the filter at the cut-off frequency f_c is 0.5, which corresponds to -6 dB.

For designing a filterbank with multiple cut-off frequencies $f_{c_1}, f_{c_2}, \ldots, f_{c_M}$, it is desirable that two consecutive transition bands do not overlap, i.e., $\alpha f_{c_i} + \alpha f_{c_{i+1}} < f_{c_{i+1}} - f_{c_i}$, $1 \leq i < M$. Hence, we must choose $\alpha = \min_i\left(\frac{f_{c_{i+1}} - f_{c_i}}{f_{c_{i+1}} + f_{c_i}}\right)$.

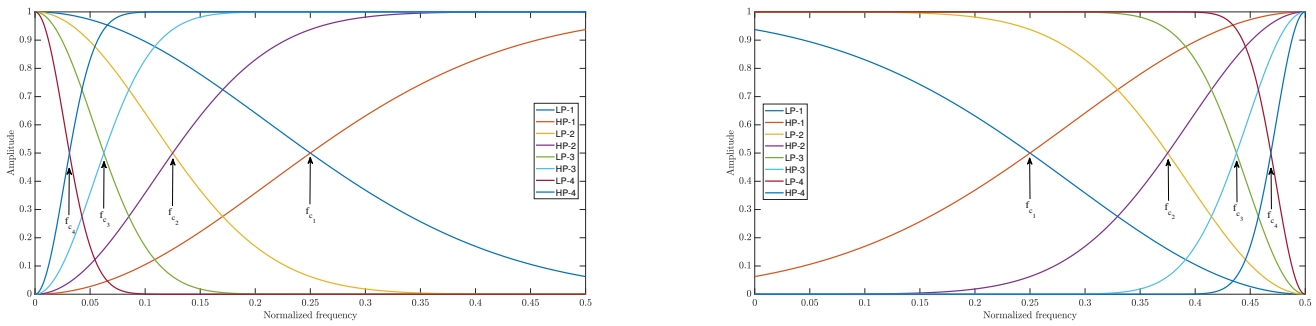

Fig. 4. Four pairs of the Gaussian lowpass (LP) and highpass (HP) filters with $F_s = 1$ and cut-off frequencies: (left) $f_{c_1} = F_s/4$, $f_{c_2} = F_s/8$, $f_{c_3} = F_s/16$, $f_{c_4} = F_s/32$; (right) $f_{c_1} = F_s/4$, $f_{c_2} = 3F_s/8$, $f_{c_3} = 7F_s/16$, $f_{c_4} = 15F_s/32$.

5) Dual of an exponential filter: We consider m times convolution of the function $\frac{\alpha}{2}\exp(-\alpha|t|)$ and its FT as

$$g(t) = \left(\frac{\alpha}{2}\exp(-\alpha|t|) * \frac{\alpha}{2}\exp(-\alpha|t|) * \cdots * \frac{\alpha}{2}\exp(-\alpha|t|)\right),$$
$$G(f) = \left(\frac{\alpha^2}{\alpha^2 + 4\pi^2 f^2}\right)^m, \quad \alpha > 0, \tag{33}$$

where $(*)$ denotes the convolution operation and $m \geq 1$ is a free parameter which determines the roll-off of the filter. Therefore, similar to FGD (27), we can define LPF and HPF as

$$G(f) = \left[\frac{1}{1 + \left(\frac{f}{f_c}\right)^2 \left(a^{1/2m} - 1\right)}\right]^m, \qquad H(f) = 1 - G(f),$$
$$f_c = \frac{\alpha\sqrt{(a^{1/2m} - 1)}}{2\pi}. \tag{34}$$

In order to obtain the same f_c for both the LP and HP filters, we use $a = 4$ which corresponds to -6 dB bandwidth. Using the central limit theorem, we observe that filter $G(f)$ defined in (34) becomes a Gaussian filter for large values of m.

6) Other desired filters: Motivated by the generalized Gaussian filter (21) and Butterworth (27), we hereby define the following generalized filters as

$$G_1(f) = \frac{1}{1 + \left(\frac{|f-\mu|}{\sigma}\right)^m}, \; G_2(f) = \frac{2}{1 + \exp\left(\frac{|f-\mu|}{\sigma}\right)^m} \tag{35}$$

where μ, σ, and m are location, scale and shape parameters, respectively. The filters defined in (35), with $\mu = 0$, can be written as

$$G_1(f) = \frac{1}{1 + \left|\frac{f}{f_c}\right|^m (\sqrt{a} - 1)},$$
$$\text{and} \quad G_2(f) = \frac{2}{1 + \exp\left(\left|\frac{f}{f_c}\right|^m \ln(2\sqrt{a} - 1)\right)}, \tag{36}$$

respectively. Similar to a Butterworth filter, these filters are maximally flat. This can be easily shown by considering any even value of m, i.e., $m = 2p$ and $p \in \mathbb{Z}^+$.

The filters defined in (18), (30) and (34) do not have ripples in either the time domain or the frequency domain. Hence, filters obtained by their extension in the 2-D space (two-dimensional space) can be used for image decomposition without any ringing artifacts.

D. Fourier–Hilbert spectrum and Narrow–band Fourier representation

The analytic signal representation of the decomposition (14) can be defined as

$$z[n] = \sum_{i=1}^{M+1}\left(\tilde{d}_i[n] + j\tilde{d}_{hi}[n]\right) = \sum_{i=1}^{M+1} a_i[n]\exp(j\phi_i[n]), \tag{37}$$

where $a_i[n] = \sqrt{\left(\tilde{d}_i[n]\right)^2 + \left(\tilde{d}_{hi}[n]\right)^2}$, $\phi_i[n] = \text{atan2}\left(\tilde{d}_{hi}[n], \tilde{d}_i[n]\right)$, and $\tilde{d}_{hi}[n]$ is the discrete Hilbert transform (HT) of $\tilde{d}_i[n]$ obtained using the FFT algorithm. The function atan2() returns the principal value of the angle in the interval $(-\pi, \pi]$ by considering the signs of both arguments to determine the quadrant of the result. The frequency $\omega_i[n] = 2\pi f_i[n]$ can be computed from $\phi_i[n]$ after phase unwrapping [33] using the forward finite difference, $\omega_i[n] = (\phi_i[n+1] - \phi_i[n])$, or backward finite difference, $\omega_i[n] = (\phi_i[n] - \phi_i[n-])$, or central finite difference, $\omega_i[n] = (\phi_i[n+1] - \phi_i[n-1])/2$. The Fourier–Hilbert spectrum (FHS) is obtained by plotting $\{n, f_i[n], a_i^2[n]/2\}$ for $1 \leq i \leq M+1$, and the energy E_d of a zero-mean signal $d[n]$ is preserved in the proposed decomposition as

$$E_d = \sum_{n=0}^{N-1} d^2[n] = \sum_{i=1}^{M+1}\sum_{n=0}^{N-1}\frac{1}{2}\left(\tilde{d}_i[n] + \tilde{d}_{hi}[n]\right)^2. \tag{38}$$

If $d[n]$ is not a zero-mean signal, then computation of the energy of signal in (38) gets modified as

$$E_d = \sum_{n=0}^{N-1} d^2[n] = \sum_{i=1}^{M+1}\sum_{n=0}^{N-1}\frac{1}{2}\left(\tilde{d}_i[n] + \tilde{d}_{hi}[n]\right)^2 + \frac{E_{dc}}{2}, \tag{39}$$

where E_{dc} is the energy corresponding to mean or DC component of the signal. This modification is needed because the Hilbert transform of a constant is zero, thus, it kills the DC component of signal.

The narrow–band inverse Fourier transform (NBIFT) or narrow–band Fourier representation (NBFR) generates narrow–band Fourier spectrum by utilizing a large number of uniform bands (for example, 200 uniform bands in Figure 5 (vii)) and then plotting these bands in the time-frequency plane as $\{n, f_i, \tilde{d}_i^2[n]\}$ for $1 \leq i \leq M+1$, where frequency resolution

is $(F_s/2(M+1))$ and $f_i = i \times [(F_s/2(M+1))]$. The signal energy E_d is preserved in the proposed decomposition as

$$E_d = \sum_{n=0}^{N-1} d^2[n] = \sum_{i=1}^{M+1} \sum_{n=0}^{N-1} \left(\tilde{d}_i[n]\right)^2. \tag{40}$$

The NBFR can be obtained by using any of the filtering schemes discussed in the previous section while considering uniform frequency bands.

E. The 2D-FGD for Images

For the decomposition of two dimensional (2D) signals (e.g., images), we design the 2D generalized Gaussian zero-phase LPF and HPF using the outer product as follows:

$$G[k,l] = \exp\left(-\left(\frac{k}{k_c}\right)^p \ln\left(\sqrt{a}\right)\right) \exp\left(-\left(\frac{l}{l_c}\right)^q \ln\left(\sqrt{a}\right)\right),$$
$$\text{and} \quad H[k,l] = 1 - G[k,l], \tag{41}$$

where $k = 0, 1, 2, \ldots, M-1$, $l = 0, 1, 2, \ldots, N-1$, and $a = 2$ corresponds to -6 dB bandwidth. A higher value of free parameters p and q provides a sharper roll-off.

The two-dimensional DCT-2 and inverse DCT-2 pairs of a sequence, $d[m,n]$, are defined as [31]

$$D[k,l] = \sum_{m=0}^{M-1} \sum_{n=0}^{N-1} \sigma_k \sigma_l d[m,n] \cos\left(\frac{\pi k(2m+1)}{2M}\right) \times \cos\left(\frac{\pi l(2n+1)}{2N}\right), \tag{42}$$

and

$$d[m,n] = \sum_{k=0}^{M-1} \sum_{l=0}^{N-1} \sigma_k \sigma_l D[k,l] \cos\left(\frac{\pi k(2m+1)}{2M}\right) \times \cos\left(\frac{\pi l(2n+1)}{2N}\right), \tag{43}$$

respectively. Using the proposed methodology, we can decompose an image $d[m,n]$ into a set of 2D-FIBFs as

$$d[m,n] = \sum_{i=1}^{M} d_i[m,n], \tag{44}$$

where $d_i[m,n]$ are obtained using the filter $G_i[k,l]$ defined in (41), i.e.,

$$d_i[m,n] = \sum_{k=0}^{M-1} \sum_{l=0}^{N-1} \sigma_k \sigma_l D[k,l] G_i[k,l] \cos\left(\frac{\pi k(2m+1)}{2M}\right) \times \cos\left(\frac{\pi l(2n+1)}{2N}\right). \tag{45}$$

IV. Results and discussion

In this section, we present many applications of the proposed methodology and compare the results with the existing state-of-the-art techniques. The generalized Gaussian filterbanks have been used to obtain results with the proposed methodology. The results obtained by the generalized Butterworth, raised cosine, and the other defined filer banks are mathematically different, but they visually look similar. Therefore, these plots are not included in the simulation results.

A. Time-frequency analysis

In this subsection, we consider a synthetic signal $s(t)$ in the time interval $0 \le t \le 10$ as

$$s(t) = x(t) + x(10-t), \tag{46}$$

where $x(t) = \sin\left(2\pi 500t + 40\pi t^2\right) + \sin\left(3\pi t^3\right) + 2\sin(2\pi 112.5t) + \sin(2\pi 500t) + \sin(2\pi 600t) + \sin(2\pi 700t) + \sin(2\pi 800t)$, and sampling frequency $F_s = 2000$ Hz.

In order to demonstrate the performance of the proposed methodology, we compare it with the existing state-of-the-art approaches for signal decomposition and time-frequency analysis. A comparative time-frequency analysis of the signal $y(t)$ is shown in Figure 5 where: (i) Synthetic signal (first-row top-left) and its Fourier spectrum (first-row bottom-left), (ii) EMD Hilbert spectrum (first-row right-side), (iii) Continuous wavelet transform (CWT) Scalogram (second-row left-side), (iv) Wavelet synchrosqueezed transform (WSST) (second-row right-side), (v) STFT (third-row left-side), (vi) Fourier synchrosqueezed transform (FSST) (third-row right-side), (vii) Proposed narrowband Fourier representation (NBFR) (fourth-row left-side), and (viii) Proposed Fourier-Hilbert spectrum (FHS) (fourth-row right-side). We have used 200 uniform bands to obtain the results with proposed method. The EMD fails to show the embedded structures of the signal. The CWT and WSST reveal the low-frequency structures but fail for high-frequency structures. The STFT and FSST reveal the embedded structures; however, there is visible energy spreading in the time-frequency plane. The time-frequency representations (TFRs) obtained by the proposed methods NBFR and FHS are able to reveal the real structures of the considered signal with minimum energy spreading in the time-frequency plane.

B. Trend and variability estimation for prediction of COVID-19 pandemic

COVID-19 is an infectious pulmonary diseases which originated in Wuhan, China in 2019 and spread to more than 180 countries. It led to more than 4 million deaths by July 2021 and pushed millions into poverty. In order to take timely and effective decisions, it became important to model and forecast the prevalence and incidence of the disease. In the literature, various modeling schemes have been used for the same such as an auto-regressive integrated moving average (ARIMA) model [34], susceptible-infected-removed (SIR) model [35], composite Gaussian growth model [36], composite Logistic growth model [37], and dictionary learning based models [38]. In this work, we first estimated the trend of the time series data using the proposed FGD and modeled the same using an ARIMA model for forecasting. The obtained model is then used for forecasting. ARIMA(p,d,q) model for a non-stationary signal, $x(t)$, can be expressed as follows:

$$\begin{aligned} &s(t) = x(t) - x(t-1), \\ &s(t) - \alpha_1 s(t-1) - \cdots - \alpha_p s(t-p) \\ &= e(t) - \beta_1 e(t-1) - \cdots - \beta_q e(t-q). \end{aligned} \tag{47}$$

In the first step, differencing of the non-stationary signal $x(t)$ is used to obtain a stationary signal $s(t)$. This step might be repeated d times to obtain a stationary output which can then

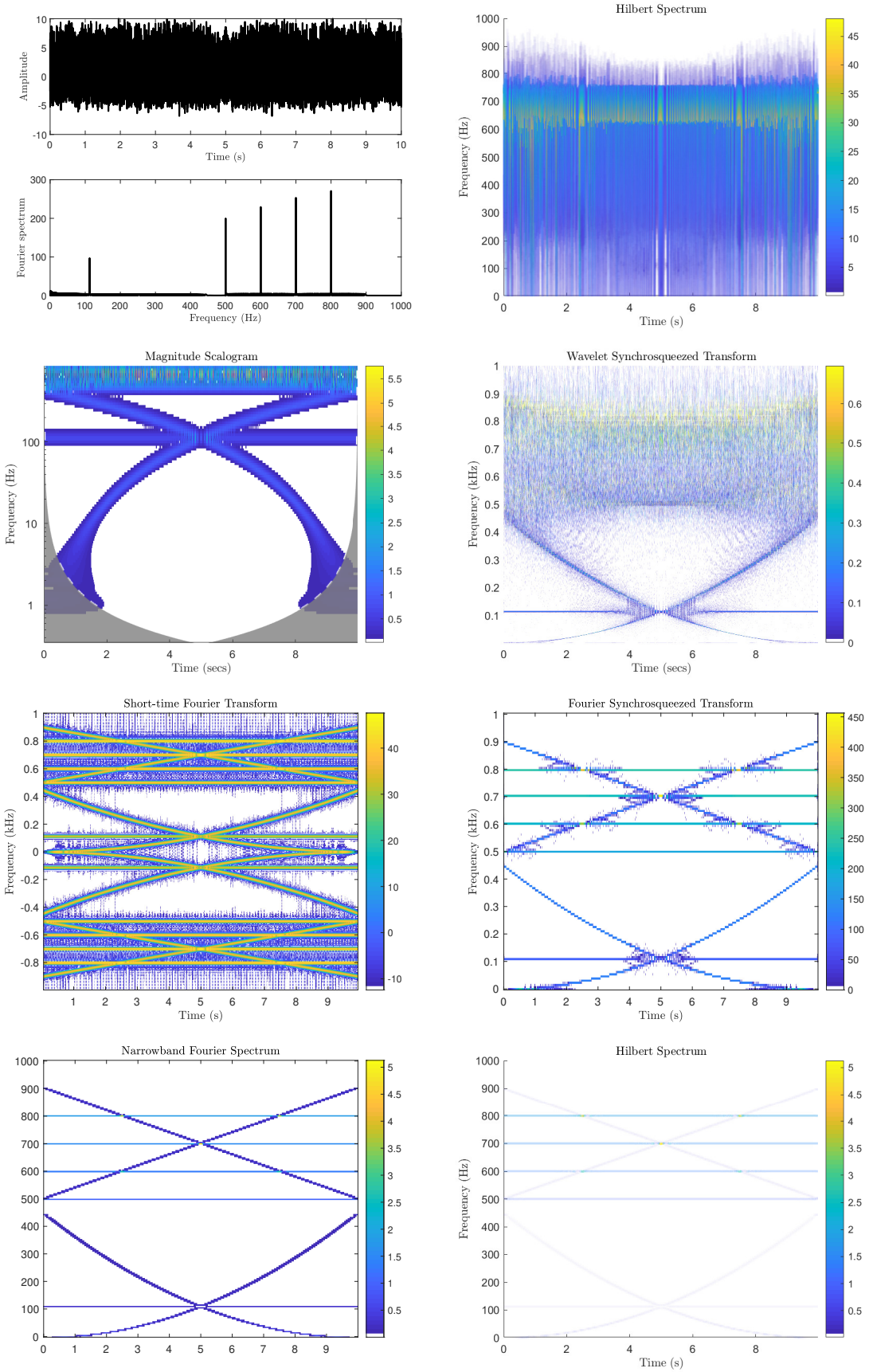

Fig. 5. A comparative time-frequency analysis: (i) Synthetic signal (first-row top-left) and its Fourier spectrum (first-row bottom-left), (ii) EMD Hilbert spectrum (first-row right-side), (iii) CWT Scalogram (second-row left-side), (iv) Wavelet synchrosqueezed transform (second-row right-side), (v) STFT (third-row left-side), (vi) Fourier synchrosqueezed transform (third-row right-side), (vii) Proposed narrowband Fourier representation (fourth-row left-side), and (viii) Proposed Fourier-Hilbert spectrum (fourth-row right-side).

be modelled using an ARMA model (47), where the AR model coefficients are represented by α_k, MA coefficients are denoted by β_k, and $e(t)$ is the error signal.

The time-series data modeled and predicted included the daily infected cases, cumulative recovered data, and cumulative death cases from India. Figure 6 presents two week forecast from July 1, 2021 to July 14, 2021 of daily COVID-19 infections (left), cumulative death cases (middle), and cumulative recovered cases (right) for India using the proposed method considering data from February 15, 2020 to June 30, 2021 [39]. Figure 7 shows actual data and the estimated values as obtained using FGD and ARIMA for daily COVID-19 infections (left), death cases (middle), and recovered cases (right) for India considering data from February 15, 2020 to June 30, 2021.

C. El Centro Earthquake time series Analysis

In May 1940, El Centro (or Imperial Valley) earthquake occurred in southern California with a magnitude of 7.1, killing nine people and causing damage to about 80 percent of the buildings. The irrigation and the railroad systems over the valley also suffered heavy damage. The towns of Imperial, Brawley, Calexico, El Centro, and Mexicali witnessed substantial losses of property. The shock also resulted in the formation of a surface rupture of 64 km on the Imperial Fault.

In this example, we consider the time-frequency-energy (TFE) estimation of the El Centro Earthquake time series [40]. The East-West, North-South, and Up-Down recordings from the earthquake, sampled at 50 Hz, and the corresponding Fourier spectrum are depicted in Fig. 8, 9 and 10, respectively. They can be categorized as nonlinear and nonstationary. From the power spectral densities (PSDs) of East-West and North-South recordings, it is observed that the majority of the energy is present in the frequency range 0–10 Hz. Moreover, from the PSD of Up-Down recordings, one can observe that energies are higher around 8 Hz and are significantly spread over 0–25 Hz. These frequencies are critical in the design of various structures. The TFE distributions of these recordings obtained by the proposed methods, namely narrowband Fourier representation (NBFR) and Fourier-Hilbert spectrum (FHS) with 50 uniform bands, are also shown in the Figures 8, 9, and 10. The TFE distributions of East-West and North-South indicate that the maximum energy concentration in the signal is around 2 seconds and 1.7 Hz, and Up-Down indicates an energy concentration of around 2 seconds and 8 Hz. These TFE distributions provide details of how the different waves arrive from the epical center to the recording station, e.g., the compression waves of small amplitude, but higher frequency range of 10–20 Hz, the shear and surface waves of strongest amplitude and lower frequency range of below 5 Hz which does most of the damage, and other body shear waves which are present over the full duration of the data span.

D. Time-frequency analysis of Gravitation wave GW150914

In 1916, Albert Einstein predicted the existence of gravitation waves (GWs) using the general theory of relativity. These waves are ripples in the space-time continuum that travel at the speed of light outward from a source. After the prediction of almost 100 years, the laser interferometer gravitational-wave observatory (LIGO) captured the first transient Gravitational wave GW150914 on September 14, 2015, at 09:50:45 UTC. This wave was generated by the merger of two black holes nearly 1.3 billion light-years away. In the history of human life, the GW150914 event marks one of the greatest scientific discoveries and opened the floodgates for probing cataclysmic events in the universe, such as cosmic inflation and the mergers of binary black holes or neutron stars.

We present the time-frequency representation (TFR) of the first GW wave generated by a binary black hole merger event [41]. The GW150914 data has been downloaded from the GW open science center [42]. Instantaneous frequency (IF) is used to calculate many parameters of a recorded event, such as separation, primary mass, secondary mass, total mass, chirp mass, velocity, luminosity distance, and effective spin of binary black hole merger. Therefore, an accurate estimation of IF is of paramount importance. The amplitude strain of GW150914 event increases to the peak value of 1.0×10^{-21}, and the frequency of the wave sweeps upwards from 35 Hz to 250 Hz [41]. Figure 11 presents (a) LIGO Hanford (H1) GW strain amplitude obtained by numerical relativity model without filter (left top) and its Fourier spectrum (left bottom), and (b) Hilbert spectrum without any decomposition which has many unwanted fluctuations in the estimated IF. The GW150914 data decomposition and TFR are presented in Figure 12 (a) a set of six IMFs and residue generated by EMD algorithm (left top), (b) a set of six FIBFs [FIBF-1: 0–10 Hz, FIBF-2: 10–350 Hz, FIBF-3: 350–500 Hz, FIBF-4: 500–700 Hz, FIBF-5: 700–4096 Hz, FIBF-6: 4096–8192 Hz] obtained from the proposed FGD (right top), (c) EMD Hilbert spectrum (left bottom), and (d) proposed FGD Hilbert spectrum (right bottom) where unwanted fluctuations are suppressed significantly in IF estimation. Thus, the TFR obtained by the proposed method reveals the real nature of the GW event and also provides a better IF estimation than the EMD algorithm.

E. Image decomposition

We now extend our results for the proposed method by considering 2D data or images. Image decomposition using the proposed scheme is depicted in Fig. 13 with (a) Four isotropic Gaussian 2D PR filters (top-left) LP–LP, (top-right) LP–BP_1, BP_1–LP, BP_1–BP_1, (bottom-left) LP–BP_2, BP_2–LP, BP_2–BP_2, and (bottom-right) LP–HP, HP–LP, HP–HP filters with $F_s = 1$ and cut-off frequencies: LP: $[0$–$F_s/64]$, BP_1: $[F_s/64$–$F_s/16]$, BP_2: $[F_s/16$–$F_s/4]$, and HP: $[F_s/4$–$F_s/2]$; (b) Original image, FIBF-1 to FIBF-4 corresponding to four filters, and recovered image obtained by sum of all FIBFs. The filters have been designed in such a manner that the BP filters would appear as rings in the 2D frequency plot. The LP–LP considers only the low-frequency components present across both the directions (horizontal and vertical), i.e., it would reject all the frequency components in the horizontal or vertical direction, lying above the cut-off frequency $F_s/64$. Further, a combination of the first two filters would result in LP–LP with a higher cut-off frequency of the BP_1, i.e., $F_s/16$ in the above example. Hence, the second filter captures all the frequency components in the image, where either or both the frequencies (horizontal and/or vertical) lie between the two cut-off frequencies. The last filter ensures that at least one of the frequencies is high. The number of filters and the corresponding cut-off frequencies may be chosen as per

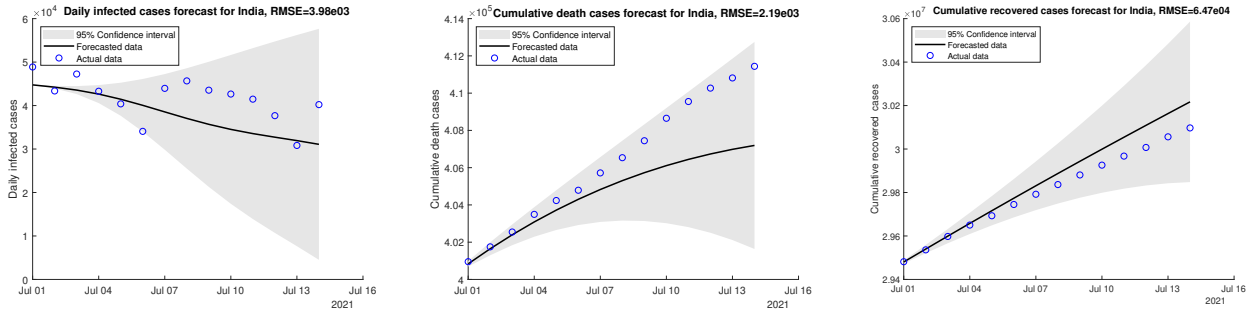

Fig. 6. Two week forecast from July 1, 2021 to July 14, 2021 of (left) daily COVID-19 infections, (middle) cumulative death cases, and (right) cumulative recovered cases for India using the proposed method considering data from February 15, 2020 to June 30, 2021.

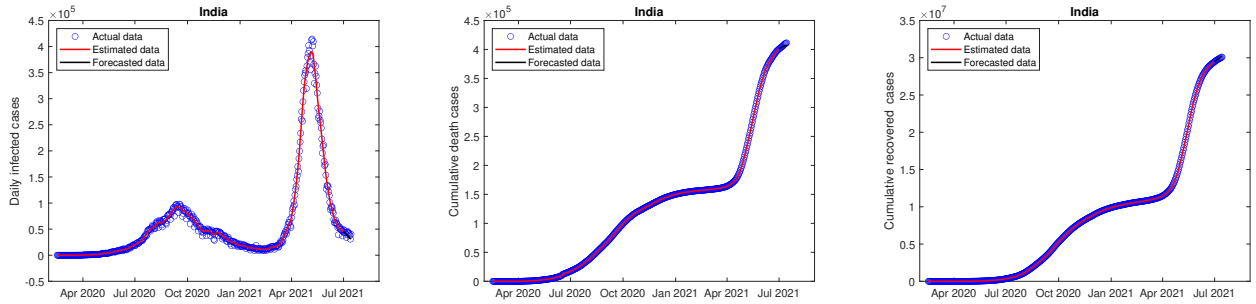

Fig. 7. Actual data and the estimated values as obtained using FGD and ARIMA for (left) daily COVID-19 infections, (middle) death cases, and (right) recovered cases for India considering data from February 15, 2020 to June 30, 2021.

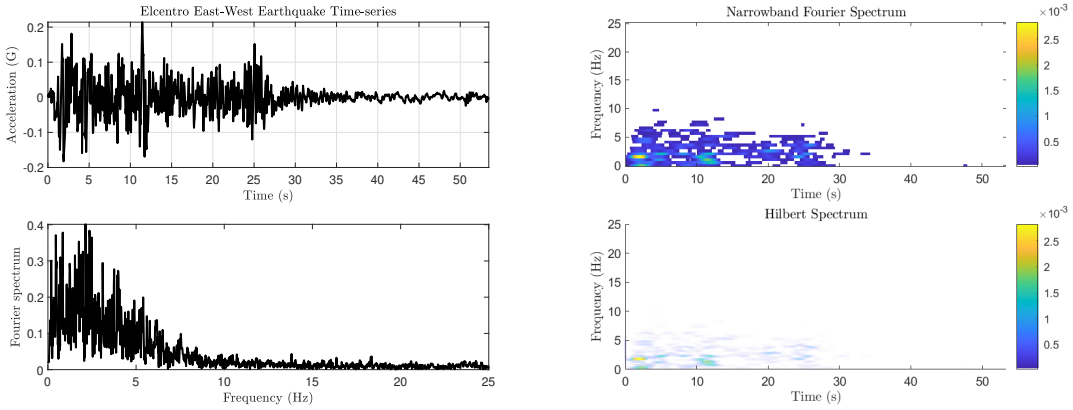

Fig. 8. The El Centro East-West earthquake time series (top left), Fourier spectrum (bottom left), proposed narrowband Fourier spectrum (top right) and Fourier–Hilbert spectrum (bottom right).

the application. Perfect reconstruction is ensured in all cases, irrespective of the choice of cut-off frequencies or the filtering method.

V. Conclusion

This work presents a perfect reconstruction filterbank representation with the flexibility to choose cut-off frequencies as per pre-defined schemes, such as uniform or dyadic frequency bands, and also using automated algorithms deriving significant frequencies from the Fourier spectrum. While different filtering schemes have been provided in this work, a generic procedure has been derived to ensure perfect reconstruction in all the cases. The synthesis stage is reduced to the simple addition of the signal components. Moreover, the proposed approach preserves the energy of the signals in the decomposition, which is vital in the time-frequency-energy analysis of many physical phenomena. Specifically, the adaptive Fourier–Gauss decomposition (FGD) and adaptive Fourier–Butterworth decomposition (FBD) have been proposed as robust signal processing techniques for nonlinear and nonstationary time series acquired from the real world. These methods allow for appropriate separation of signal components, thereby providing a method to extract specific desirable components and remove noises. The strength of the proposed techniques is validated across many synthetic as well as real-life signals.

References

[1] J. B. J. Fourier, "Théorie de la propagation de la chaleur dans les solides," *Manuscrispt submitted to the Institute of France*, 21 Dec. 1807.

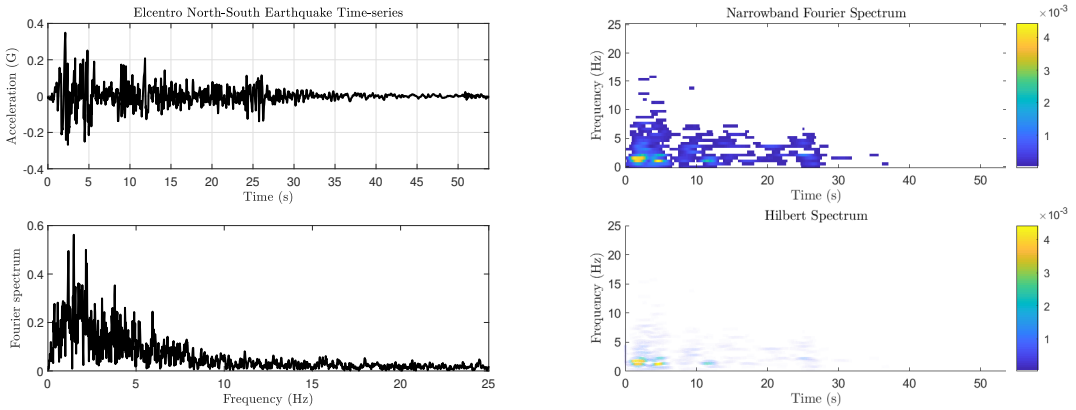

Fig. 9. The El Centro North-South earthquake time series (top left), Fourier spectrum (bottom left), proposed narrowband Fourier spectrum (top right) and Fourier–Hilbert spectrum (bottom right).

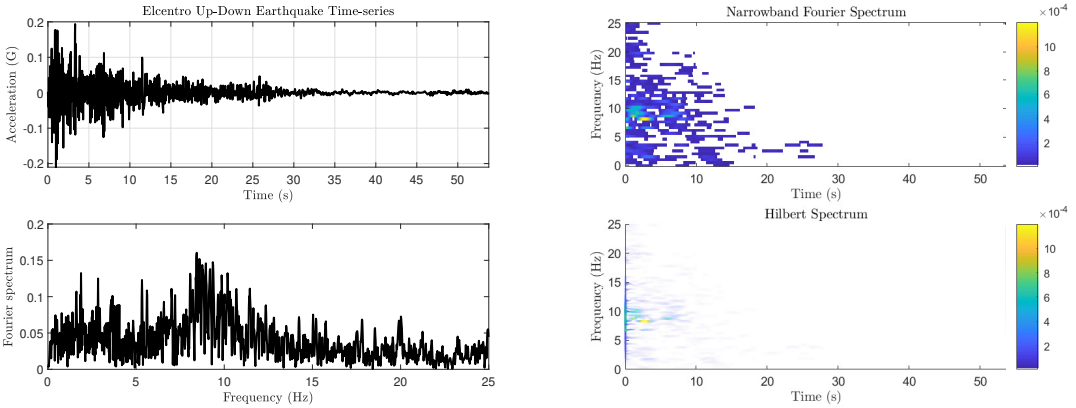

Fig. 10. The El Centro Up-Down earthquake time series (top left), Fourier spectrum (bottom left), proposed narrowband Fourier spectrum (top right) and Fourier–Hilbert spectrum (bottom right).

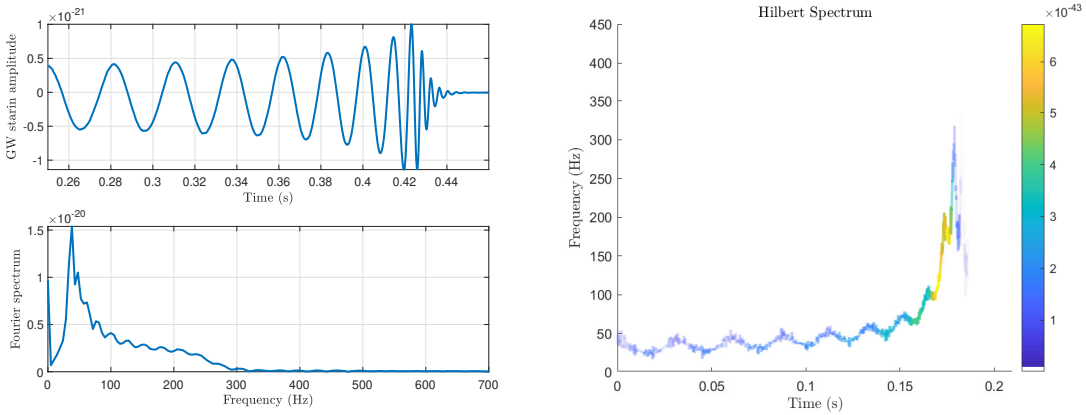

Fig. 11. The GW150914 data analysis (a) LIGO Hanford (H1) GW strain amplitude obtained by numerical relativity model without filter (left top) and its Fourier spectrum (left bottom), and (b) Hilbert spectrum without any decomposition.

[2] ——, "Théorie du mouvement de la chaleur dans les corps solides," *Mémoires de l´Académie royale des sciences de l´Institute de France*, vol. no. 4, 1811.

[3] ——, "Théorie analytique de la chaleur," *Paris: Chez Firmin Didot, Pére et Fils*, 1822.

[4] P. Singh, A. Gupta, and S. D. Joshi, "General parameterized fourier transform: A unified framework for the fourier, laplace, mellin and z transforms," *IEEE Transactions on Signal Processing*, vol. 70, pp. 1295–1309, 2022.

[5] F. Hlawatsch and G. Boudreaux-Bartels, "Linear and quadratic time-frequency signal representations," *IEEE Signal Process. Mag.*, vol. 9, pp. 21–67, 1992.

[6] D. Gabor, "Theory of communications," *Journal on IEE*, vol. 93, pp. 429–457, 1946.

[7] I. Daubechies, "Orthonormal basis of commonly supported wavelets," *Communications on Pure and Applied Mathematics*, vol. 41, pp. 909–996, 1988.

[8] A. Gupta, S. D. Joshi, and S. Prasad, "A new approach for estimation of statistically matched wavelet," *IEEE transactions on signal processing*, vol. 53, no. 5, pp. 1778–1793, 2005.

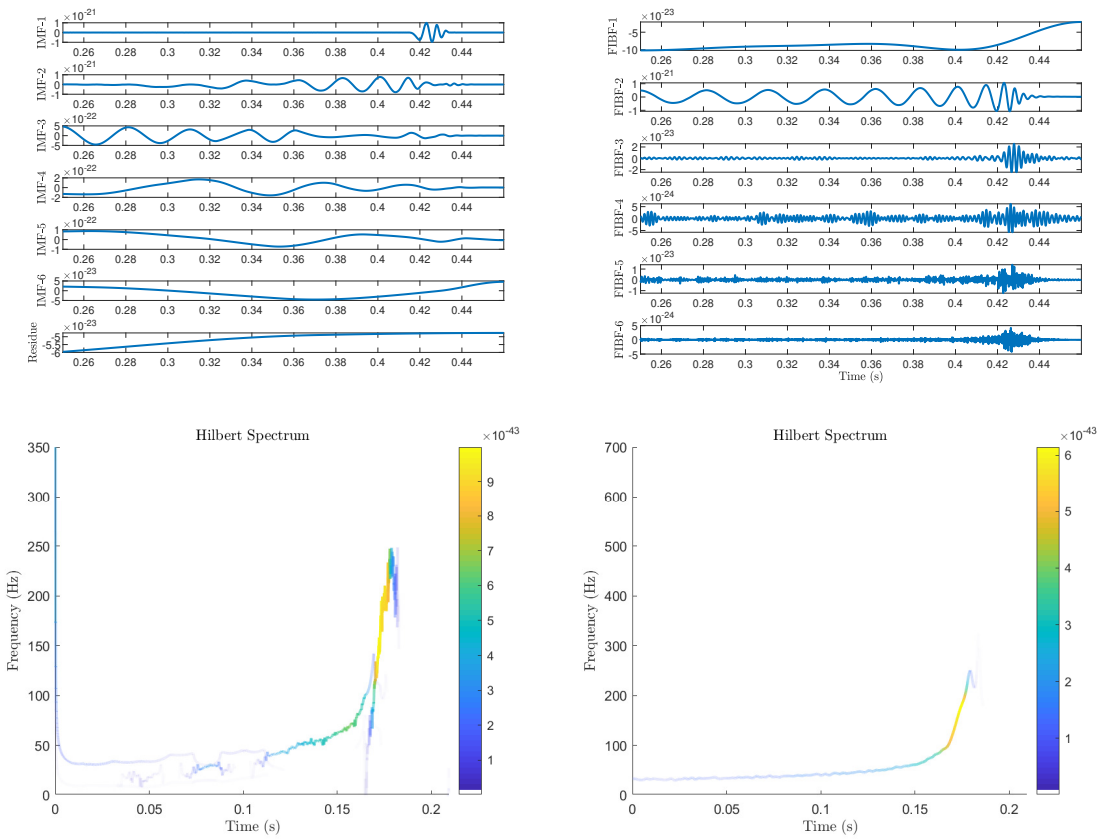

Fig. 12. The GW150914 data analysis (a) a set of six IMFs and residue generated by EMD algorithm (left top), (b) a set of six FIBFs obtained from the proposed FGD (right top) with considered set of bands $\{[0, 10), [10, 350), [350, 500), [500, 700), [700, F_s/4], (F_s/4, F_s/2]\}$ Hz where $F_s = 16384$ Hz, (c) EMD Hilbert spectrum (left bottom), and (d) proposed FGD Hilbert spectrum (right bottom).

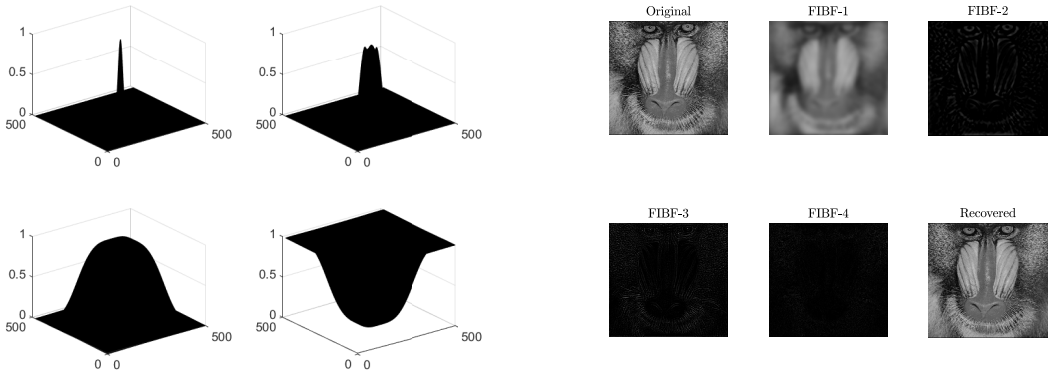

Fig. 13. The FFT based image decomposition (a) Four isotropic Gaussian 2D PR filters (top-left) LP–LP, (top-right) LP–BP_1, BP_1–LP, BP_1–BP_1, (bottom-left) LP–BP_2, BP_2–LP, BP_2–BP_2, and (bottom-right) LP–HP, HP–LP, HP–HP filters with $F_s = 1$ and cut-off frequencies: LP: $[0$–$F_s/64]$, BP_1: $[F_s/64$–$F_s/16]$, BP_2: $[F_s/16$–$F_s/4]$, and HP: $[F_s/4$–$F_s/2]$; (b) Original image, FIBF-1 to FIBF-4 corresponding to four filters, and recovered image obtained by sum of all FIBFs.

[9] ——, "A new method of estimating wavelet with desired features from a given signal," *Signal Processing*, vol. 85, no. 1, pp. 147–161, 2005.

[10] N. E. Huang, Z. Shen, S. R. Long, M. C. Wu, H. H. Shih, Q. Zheng, N.-C. Yen, C. C. Tung, and H. H. Liu, "The empirical mode decomposition and the Hilbert spectrum for nonlinear and non-stationary time series analysis," *Proc. R. Soc. Lond. A.*, vol. 454, pp. 903–995, 1998.

[11] Z. Wu and N. E. Huang, "Ensemble empirical mode decomposition: A noise-assisted data analysis method," *Adv. Adapt. Data Anal.*, vol. 1, no. 1, pp. 1–41, 2009.

[12] M. E. Torres, M. A. Colominas, G. Schlotthauer, and P. Flandrin, "A complete ensemble empirical mode decomposition with adaptive noise," in *2011 IEEE International Conference on Acoustics, Speech and Signal Processing (ICASSP)*, 2011, pp. 4144–4147.

[13] H.-T. W. Ingrid Daubechies, Jianfeng Lu, "Synchrosqueezed wavelet transforms: An empirical mode decomposition-like tool," *Applied and Computational Harmonic Analysis*, vol. 30, no. 2, pp. 243–261, 2011.

[14] I. W. Selesnick, "Wavelet transform with tunable q-factor," *IEEE Transactions on Signal Processing*, vol. 59, no. 8, pp. 3560–3575, 2011.

[15] K. Dragomiretskiy and D. Zosso, "Variational mode decomposition," *IEEE Transactions on Signal Processing*, vol. 62, no. 3, pp. 531–544, 2014.

[16] N. Ansari and A. Gupta, "M-RWTL: learning signal-matched rational wavelet transform in lifting framework," *IEEE Access*, vol. 6, pp. 12 213–12 227, 2018.

[17] ——, "WNC-ECGlet: Weighted non-convex minimization based reconstruction of compressively transmitted ECG using ECGlet," *Biomedical Signal Processing and Control*, vol. 49, pp. 1–13, 2019.

[18] J. Gilles, "Empirical wavelet transform," *IEEE Transactions on Signal Processing*, vol. 61, no. 16, pp. 3999–4010, 2013.

[19] P. Singh, S. D. Joshi, R. K. Patney, and K. Saha, "The Fourier decomposition method for nonlinear and non-stationary time series analysis," *Proceedings of the Royal Society of London A: Mathematical, Physical and Engineering Sciences*, vol. 473: 20160871, pp. 1–27, 2017.

[20] P. Singh, "Novel Fourier quadrature transforms and analytic signal representations for nonlinear and non-stationary time series analysis," *Royal Society Open Science*, vol. 5: 181131, pp. 1–26, 2018.

[21] A. S. Udawat and P. Singh, "An automated detection of atrial fibrillation from single-lead ecg using hrv features and machine learning," *Journal of Electrocardiology*, 2022. [Online]. Available: https://www.sciencedirect.com/science/article/pii/S0022073622001650

[22] B. Fatimah, A. Singhal, and P. Singh, "A multi-modal assessment of sleep stages using adaptive fourier decomposition and machine learning," *Computers in Biology and Medicine*, vol. 148, p. 105877, 2022. [Online]. Available: https://www.sciencedirect.com/science/article/pii/S0010482522006278

[23] B. Fatimah, P. Singh, A. Singhal, D. Pramanick, P. S., and R. B. Pachori, "Efficient detection of myocardial infarction from single lead ecg signal," *Biomedical Signal Processing and Control*, vol. 68, p. 102678, 2021. [Online]. Available: https://www.sciencedirect.com/science/article/pii/S1746809421002755

[24] B. Fatimah, P. Singh, A. Singhal, and R. B. Pachori, "Hand movement recognition from semg signals using fourier decomposition method," *Biocybernetics and Biomedical Engineering*, vol. 41, no. 2, pp. 690–703, 2021. [Online]. Available: https://www.sciencedirect.com/science/article/pii/S0208521621000346

[25] A. Singhal, P. Singh, B. Lall, and S. D. Joshi, "Modeling and prediction of covid-19 pandemic using gaussian mixture model," *Chaos, Solitons & Fractals*, vol. 138, p. 110023, 2020. [Online]. Available: https://www.sciencedirect.com/science/article/pii/S0960077920304215

[26] B. Fatimah, P. Singh, A. Singhal, and R. B. Pachori, "Detection of apnea events from ecg segments using fourier decomposition method," *Biomedical Signal Processing and Control*, vol. 61, p. 102005, 2020. [Online]. Available: https://www.sciencedirect.com/science/article/pii/S1746809420301610

[27] A. Singhal, P. Singh, B. Fatimah, and R. B. Pachori, "An efficient removal of power-line interference and baseline wander from ecg signals by employing fourier decomposition technique," *Biomedical Signal Processing and Control*, vol. 57, p. 101741, 2020. [Online]. Available: https://www.sciencedirect.com/science/article/pii/S1746809419303222

[28] P. Singh, A. Singhal, B. Fatimah, A. Gupta, and S. D. Joshi, "AF-MNS: A novel AM-FM based measure of non-stationarity," *IEEE Communications Letters*, vol. 25, no. 3, pp. 990–994, 2021.

[29] P. Singh, A. Singhal, B. Fatimah, and A. Gupta, "System and method for nonlinear and non-stationary time-series analysis using adaptive Fourier–Gauss decomposition, patent, lodged January," 2022.

[30] N. Ahmed, T. Natarajan, and K. R. Rao, "Discrete cosine transform," *IEEE Trans. Computers*, pp. 90–93, 1974.

[31] V. Britanak, P. C. Yip, and K. R. Rao, "Discrete cosine and sine transforms: General properties," *Fast algorithms and Integer Approximations*, 2006.

[32] S. S. Butterworth, "On the theory of filter amplifiers," *Experimental Wireless and the Wireless Engineer*, vol. 7, pp. 536–541, 1930.

[33] P. Singh, "Breaking the limits: Redefining the instantaneous frequency," *Circuits Syst Signal Process*, vol. 37, pp. 3515–3536, 2018.

[34] G. Box and G. M. Jenkins, *Time Series Analysis: Forecasting and Control*. Holden-Day, 1976.

[35] H. W. Hethcote, "The mathematics of infectious diseases," *SIAM Review*, vol. 42, no. 4, pp. 599–653, 2000.

[36] J. Schuttler, R. Schlickeiser, F. Schlickeiser, and M. Kröger, "Covid-19 predictions using a gauss model, based on data from april 2," *Physics*, vol. 2, no. 2, pp. 197–212, 2020.

[37] P. Wang, X. Zheng, J. Li, and B. Zhu, "Prediction of epidemic trends in COVID-19 with logistic model and machine learning technics," *Chaos, Solitons & Fractals*, vol. 139, p. 110058, 2020.

[38] H. Lyu, C. Strohmeier, G. Menz, and D. Needell, "COVID-19 Time-series Prediction by Joint Dictionary Learning and Online NMF," *arXiv e-prints*, p. arXiv:2004.09112, Apr. 2020.

[39] Worldometers, "Worldometers," 2020, Retrieved: June 30, 2021.

[40] "Vibrationdata: El Centro Earthquake," http://www.vibrationdata.com/elcentro.htm, Accessed: 15-06-2021.

[41] B. A. et al., "Observation of gravitational waves from a binary black hole merger," *Phys. Rev. Lett.*, vol. PRL 116, p. 061102, 2016.

[42] "Gravitational Wave Open Science Center," https://losc.ligo.org/events/GW150914/, Accessed: 14-07-2021.